

# Multifrequency study of the Large Magellanic Cloud supernova remnant (SNR) B0513–692 and new SNR candidate J051327–6911

I. S. Bojičić,<sup>1\*</sup> M. D. Filipović,<sup>2</sup> Q. A. Parker,<sup>1,3</sup> J. L. Payne,<sup>4</sup> P. A. Jones,<sup>5</sup> W. Reid,<sup>1</sup> A. Kawamura<sup>6</sup> and Y. Fukui<sup>6</sup>

<sup>1</sup>*Department of Physics, Macquarie University, Sydney, NSW 2109, Australia*

<sup>2</sup>*University of Western Sydney, Locked Bag 1797, Penrith South DC, NSW 1797, Australia*

<sup>3</sup>*Anglo-Australian Observatory, PO Box 296, Epping, NSW 1710, Australia*

<sup>4</sup>*Centre for Astronomy, James Cook University, Townsville, Queensland 4811, Australia*

<sup>5</sup>*Australia Telescope National Facility, CSIRO, PO Box 76, Epping, NSW 1710, Australia*

<sup>6</sup>*Department of Astrophysics, Nagoya University, Furocho, Chikusaku, Nagoya 464–8602, Japan*

Accepted 2007 March 27. Received 2007 March 5; in original form 2006 November 15

## ABSTRACT

We present a new multiwavelength study of supernova remnant (SNR) B0513–692 in the Large Magellanic Cloud (LMC). The remnant also has a strong, superposed, essentially unresolved, but unrelated radio source at its north-western edge, J051324–691049. This is identified as a likely compact H II region based on related optical imaging and spectroscopy. We use the Australia Telescope Compact Array (ATCA) at 4790 and 8640 MHz ( $\lambda \simeq 6$  cm and  $\lambda \simeq 3.5$  cm) to determine the large-scale morphology, spectral index and polarization characteristics of B0513–692 for the first time. We detect a strongly polarized region (49 per cent) in the remnant's southern edge ( $\lambda \simeq 6$  cm). Interestingly, we also detect a small ( $\sim 40$  arcsec) moderately bright, but distinct optical, circular shell in our H $\alpha$  imagery which is adjacent to the compact H II region and just within the borders of the north-eastern edge of B0513–692. We suggest that this is a separate new SNR candidate based on its apparently distinct character in terms of optical morphology in three imaged emission lines and indicative SNR optical spectroscopy (including enhanced optical [S II] emission relative to H $\alpha$ ).

**Key words:** H II regions – supernova remnants – Magellanic Clouds – radio continuum: galaxies.

## 1 INTRODUCTION

The Large Magellanic Cloud (LMC) offers a unique opportunity for studying supernovae (SNe) and supernova remnants (SNRs) in varied environments. All objects within the LMC can be considered essentially at the same distance of  $\sim 51.5$  kpc (e.g. Feast 1999; Nelson et al. 2000) and is essentially a thin ( $\sim 500$  parsec) disc inclined at only  $35^\circ$  to our line of sight (van der Marel & Cioni 2001). This permits accurate nebular and physical parameters to be determined for LMC SNRs. Furthermore, the LMC is close enough to resolve the structure and morphology of individual extended objects contained within it, such as SNRs. These studies are enhanced by the small uncertainty in absorption towards the LMC (e.g. Kaler & Jacoby 1990).

The best approach to identify SNR candidates is through the use of multiwavelength surveys. Most commonly, these surveys include the X-ray, radio and optical domains, although SNRs also produce a large number of emission lines in the ultraviolet (UV) and infrared

(IR) wavelength regimes. In the radio, techniques to distinguish between SNRs and the other nebula types are based on their strongly polarized and non-thermal emission. SNRs have an average radio spectral index (defined as  $S_\nu \propto \nu^\alpha$ ) of  $\alpha = -0.5$  (Inglis & Kitchin 1990) compared to H II regions which have much flatter spectra of  $\alpha \sim 0$ . In the optical, narrow-band imaging at H $\alpha$ , [S II] and [O III] wavelengths can be a useful discriminant as the morphological details, such as spherical (shell) symmetry and filamentary structure is helpful in distinguishing SNRs from other sources such as H II regions and superbubbles, especially as a function of the imaged line. A comparison of their spectral emission-line signatures from spectroscopy allows us for more unequivocal identification of SNRs via specific, diagnostic line ratios, particularly [S II] relative to H $\alpha$  (e.g. Fesen, Blair & Kirshner 1985).

The first SNR radio identification in the LMC was made using the Parkes radio telescope at 1410 MHz with a resolution of about 14 arcmin (Mathewson & Healey 1964) and the most extensive work in identifying Magellanic Cloud SNRs was conducted by Mathewson et al. (1983, 1984, 1985). Recently, we have identified 76 SNRs within the LMC of which 32 are new SNR candidates (Filipović et al., in preparation). Currently, the identifications are based solely

\*E-mail: ibojcic@physics.mq.edu.au

on each object’s morphological structure from our powerful new radio mosaic images of the LMC, so additional corroborating data such as that presented here are extremely useful.

In this paper, we investigate the multiwavelength properties of one of the LMC remnants recovered in our new survey: SNR B0513–692. We do this by bringing together new and archival radio, X-ray and optical imagery, together with new optical spectroscopy and a fresh assessment of the surrounding environment.

SNR B0513–692 (J051315–691219) was first confirmed as an SNR by Mathewson et al. (1985) who studied its morphology, non-thermal radio spectra and filamentary H $\alpha$  emission.

In the radio band, they used detections from Mills & Turtle (1984) with the Molonglo Observatory Synthesis Telescope (MOST) at 843 MHz, and from Clarke, Little & Mills (1976) with Molonglo radio data at 408 MHz, to examine the radio morphology and to determine a radio spectral index of  $\alpha = -0.5$ . An initial X-ray detection of the remnant candidate was based on data obtained from the archives of the Columbia–Einstein Observatory survey of the LMC (Long, Helfand & Grabelsky 1981). In the optical they used the IPCS on the 3.9-m Anglo–Australian Telescope (AAT) coupled with narrow-band interference filters centred on key optical emission lines to image a  $3.5 \times 3.5$ -arcmin<sup>2</sup> region of the remnant. In particular they found that the [S II]/H $\alpha$  point-to-point ratio of this object was typically  $\sim 0.6$ . Such a high value is a classic signature of a likely SNR (Fesen et al. 1985). Their narrow-band observations showed the filamentary H $\alpha$  emission following the overall radio structure. They also found an intense, compact emission component at the north-east of the remnant which corresponds to a compact radio source also noted. They identified this source as a likely, unrelated, H II region.

Here, we present a more detailed multiradio frequency, multi-wavelength study of this LMC SNR and its immediate environment in order to provide a better picture of this little studied object and to shed light on the nature of the compact radio source on the north-eastern edge and its optical counterparts. We now propose that there are, in fact, two additional, separate sources on the north-eastern boundary of B0513–692. One is confirmed as the previously catalogued compact H II region DEM L109, but the other appears to be a small, unrelated, compact new SNR candidate which we designate as J051237–6911, overlapping both the H II region and the larger remnant B0513–692.

## 2 COMPILED SOURCE DATA FOR B0513–692: NEW AND ARCHIVAL

The new radio-continuum observations of SNR B0513–692 were performed in ‘snap-shot’ mode (integration time was about 0.7 h at each frequency) using the Australia Telescope Compact Array (ATCA) at 4790 and 8640 MHz on 1997 April 6. We used the 375-m array configuration which includes 10 baselines between the first and fifth antenna and additional five spacings when a 6-km antenna was used for higher-resolution imaging. Our calibration sources included PKS B1934–638 (primary flux calibrator) and PKS B0530–727 (phase calibrator).

Data reduction was performed using the MIRIAD software package (Sault & Killen 2004). Radio-continuum images of these observations are shown in Fig. 1. These images were formed using multifrequency synthesis (Sault & Wieringa 1994) and natural weighting. They were deconvolved using the CLEAN and RESTOR algorithms with primary beam correction applied using the LINMOS task. A similar procedure was used for both *U* and *Q* Stokes parameter maps. Be-

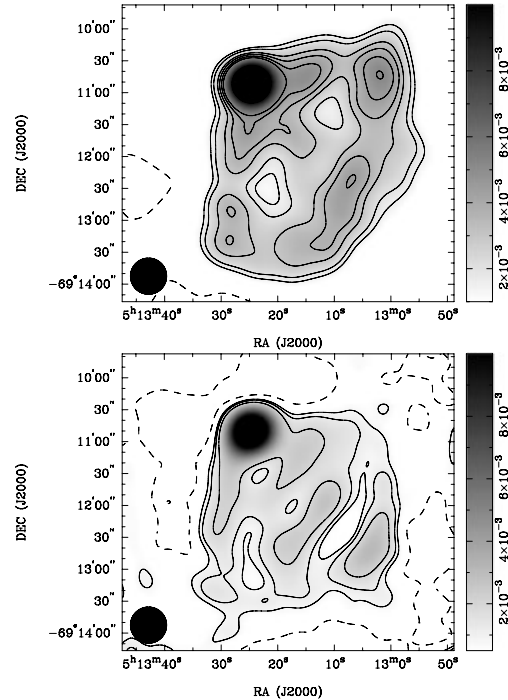


**Figure 1.** Total intensity ATCA images of SNR B0513–692 at 4790 MHz (top panel) and 8640 MHz (bottom panel), overlaid with contours giving the associated flux radio level. For the 4790-MHz image, contours include  $-1$ ,  $3$ ,  $4$ ,  $6$ ,  $7.3$ ,  $8.8$ ,  $10.3$  and  $20\sigma$  ( $\sigma = 0.5 \text{ mJy Beam}^{-1}$ ) and for the 8640-MHz image they are  $-1$ ,  $2$ ,  $3$  and  $5\sigma$  ( $\sigma = 0.4 \text{ mJy Beam}^{-1}$ ). The synthesized beam of the both ATCA observations is  $34 \times 34 \text{ arcsec}^2$  (lower left-hand corner of each image). Note the strong compact radio source at the north-eastern edge of the remnant.

cause of the low dynamic range (signal-to-noise ratio between the source flux and  $3\sigma$  noise level) self-calibration could not be applied.

A resolution of 34 arcsec was achieved at 6 cm (against 43 arcsec from Mills & Turtle 1984). Additionally, our new radio images are compared with the LMC radio maps at 3 and 6 cm from Dickel et al. (2005). Better sensitivity is achieved, especially at 3 cm, because of the longer integration time. These new data allow us to better delineate the overall shell structure and, furthermore to provide solid detection of polarized radio emission from this SNR.

The strong, compact radio source, J051324–691049, embedded within the north-eastern side of the SNR complicates the radio picture. In order to attempt to resolve this object, we used all telescope baselines (i.e. all correlations with the sixth antenna) and a Gaussian restoring beam to create a high-resolution image with a resolution of 1 arcsec at 3 cm. Unfortunately, due to the nature of the radio interferometric technique, incomplete uv coverage between the 375-m and 6-km ATCA baselines could result in over-resolving or breaking up of the source, if it is extended, into multiple point-like components. We did not find any artefacts of possible distortion, and we note that the source is either unresolved at 1 arcsec or is no larger than 19 arcsec, which is the highest resolution of the 375-m baseline at 8640 MHz. We re-analysed the ATCA data (but omitting the 6-km baseline) to yield a lower-resolution but higher-sensitivity image to enable a better study of the extended, diffuse nature of SNR B0513–692. Table 1 lists the basic radio imaging parameters. To enhance our study of the extended remnant SNR B0513–692 and the unrelated, embedded, compact source J051324–691049, we also examined existing radio data from the Sydney University

**Table 1.** Summary of the ATCA radio-continuum imaging parameters of the region – SNR B0513–692.

Frequency (MHz)	FWHM (all antennas) (arcsec <sup>2</sup> )	FWHM (6-km baseline excluded) (arcsec <sup>2</sup> )
4790	2 × 2	34 × 34
8640	1 × 1	19 × 19

Molonglo Sky Survey (SUMSS) at 843 MHz (Bock, Large & Sadler 1999) and a new ATCA mosaic image at 1377 MHz (Staveley-Smith et al., in preparation).

We also analysed new, narrow-band optical data of the SNR extracted from a deep, high-resolution H $\alpha$  map created by the digital combination (median stacking) of 12 × 2 h, narrow-band, H $\alpha$  UK Schmidt Telescope (UKST) exposures of the central 25 deg<sup>2</sup> of the LMC (Reid & Parker 2006a,b, also Section 3.2.4). This was supplemented by independent H $\alpha$ , [S II] and [O III] images from the Magellanic Cloud Emission Line Survey (MCELS) (<http://www.ctio.noao.edu/mcels/>).<sup>1</sup> These data have proven crucial in helping to unravel the nature of the compact north-eastern components (see Sections 3.2 and 3.3).

The CO map of the region comes from the NANTEN survey of the LMC (Fukui et al. 1999, 2001). IR images at 12, 25, 60 and 100  $\mu$ m were also obtained from the *Infrared All-Sky Survey (IRAS)* archive and images at 8.8  $\mu$ m from the Midcourse Space Experiment (MSX) archive. Finally, we use X-ray data from the *ROSAT* All-Sky Survey (RASS) Faint Source Catalog (Voges et al. 2000) to complete our multiwavelength data set.

### 3 ANALYSIS AND RESULTS

#### 3.1 SNR B0513–692

##### 3.1.1 Radio

The ATCA 4790-MHz radio image (Fig. 1, top panel) of SNR B0513–692 shows an elliptical ring-like structure with central features consistent with the new 1377-MHz ATCA mosaic image (Staveley-Smith et al., in preparation). The south-western part of the elliptical shell is reasonably symmetrical with peak fluxes including values of 3.65 mJy Beam<sup>-1</sup> (south-eastern contour at 7.3 $\sigma$ ), 4.4 mJy Beam<sup>-1</sup> (south-western contour at 8.8 $\sigma$ ) and 5.15 mJy Beam<sup>-1</sup> (north-western contour at 10.3 $\sigma$ ). The structure of the north-eastern half of the shell cannot be resolved since the strong, point-like source, J051324–691049, is embedded towards the north-eastern edge of the SNR. Two cavities (which are unresolved – they match the beam size) are located in the central part of the SNR with fluxes below the 4 $\sigma$  level. In Fig. 2, we show the relative intensities of slices drawn through these central cavities. Slices along the minor axis show a slightly steeper gradient on the north-eastern side of the shell which may be explained by a gradient in the surrounding interstellar medium (ISM) density or magnetic field. The shell thickness in the radio is measured at approximately 30 per cent of the object’s radius, which is probably just an upper limit considering the size of the restoring beam used.

The remnant shell in our ATCA 8640-MHz image (Fig. 1, bottom panel) was restored using a 34 × 34-arcsec<sup>2</sup> Gaussian beam and has

<sup>1</sup> The relevant 6 × 6-arcmin<sup>2</sup> fit images of the region were kindly made available to us by C. Smith et al. prior to general release.

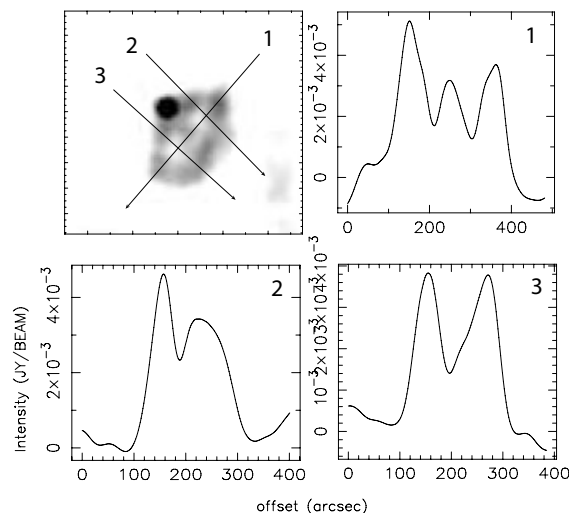


**Figure 2.** Intensity slices through SNR B0513–692. The direction of the arrows points from the left-hand to right-hand side from the zero-offset on the x-axis of the accompanying slices 1, 2 and 3.

a very low dynamic range above the surrounding noise. The unreliable contour at 2 $\sigma$  shows basic similarities to the 3 $\sigma$  contour of the 4790-MHz image, but some features including the south-western ridge are inconsistent. These regions were most likely poorly reconstructed during the cleaning stage, resulting in the formation of ‘blobs’ on the image.

The major and the minor axes are estimated from Fig. 2 to be 260 × 170 arcsec<sup>2</sup> in angular extent. Given an LMC distance of 51.5 kpc (Feast 1999; Nelson et al. 2000), this gives the linear size of the remnant as 65 × 42 pc ( $\pm 7$  pc for both axes). By comparison, optical AAT imaging in H $\alpha$  (Mathewson et al. 1985) gives dimensions of 60 × 51 pc<sup>2</sup> (using a distance to the LMC of 55 kpc).

Linear polarization images for each frequency were created using *Q* and *U* parameters. While we detect no reliable polarization at 8640 MHz, the 4790-MHz image reveals strong linear polarization in a band along the centre of the remnant and its Southern hemisphere along the rim. Fig. 3 shows areas of fractional polarization

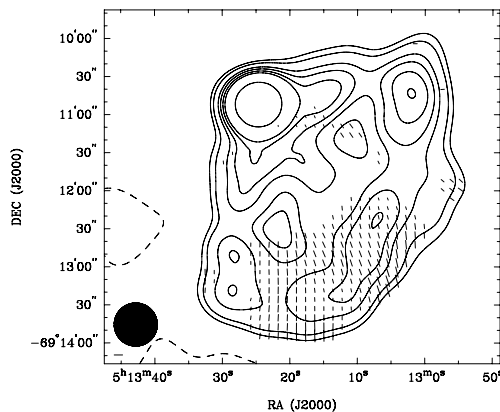


**Figure 3.** Linear polarization image of SNR B0513–692 at 4790 MHz with the same intensity contours used in Fig. 1. Polarization vectors are drawn along a band in the middle of the remnant as well as in its Southern hemisphere. The lengths of these vectors are proportional to the fractional polarization, with the highest noted at 49 per cent. This amount of fractional polarization is denoted by the bar in the lower left-hand corner of the image. Note that the correction for the Faraday rotation could not be applied (see the text).

superimposed on the same 4790-MHz intensity contours used in Fig. 1. It is the first reliable detection of polarized radio emission from this object. Polarization vectors were plotted only in those regions where the polarized intensity was greater than  $3\sigma_{q,u}$  above the noise level for the  $Q$  and  $U$  maps ( $\sigma_{q,u} = 0.1 \text{ mJy Beam}^{-1}$ ). The lengths of these vectors are proportional to the amount of fractional polarization with a maximum length corresponding to 49 per cent. The relatively small amount of linearly polarized emission on the one hand and the patchy and somewhat dubious total intensity image on the other, prevent us from detecting any significant polarization at 8640 MHz (beyond instrumentation error). Without reliable polarization measurements at the second frequency we could not determine if any Faraday rotation was present.

The mean fractional polarization at 4790 MHz was calculated using flux density and polarization:

$$P = \frac{\sqrt{S_Q^2 + S_U^2}}{S_I} 100 \text{ per cent} \quad (1)$$

where  $S_Q$ ,  $S_U$  and  $S_I$  are integrated intensities for  $Q$ ,  $U$  and  $I$  Stokes parameters. Our estimated value is  $P \cong 10$  per cent.

These results indicate the presence of a relatively strong and well-organized magnetic field with some kind of radial structure (considering the fact that the observed strong polarization intensity matches parts of the shell where the total intensity emission is also strong).

By fitting an unweighted regression line (i.e. power-law fit) at four frequencies using the flux density from our 4790-MHz observations, together with 408-, 843- (MOST) and 1377-MHz (ATCA-mosaic) flux densities (Fig. 4), we obtained a spectral index of  $-0.4 \pm 0.1$  for SNR B0513–692. This confirms the object’s non-thermal nature. Integrated flux densities and rms noise for each of these wavelengths are listed in Table 2. Our flux densities at 4790 and particularly 8640 MHz most likely represent lower limits because of the relatively short integration time. The flux density at 8640 MHz was omitted from the regression-line calculation for this reason.

Flux density errors ( $\sigma_s$ ) were estimated from:  $\sigma_s = [N \cdot \text{Noise}_{\text{rms}}^2 + (0.05 S_v)^2]^{1/2}$  (Weiler et al. 1986; Ho & Ulvestad 2001), that is, from the rms noise across the surface of a source, and from the influence of the errors in calibration. Since the calculated values range between 6 and 10 per cent, we assign 10 per cent error bars to the remainder of the flux as an upper limit of flux density errors.

### 3.1.2 Previous X-ray observations

This SNR was first detected in the Einstein survey of the LMC (Long et al. 1981) and diffuse X-ray emission from SNR B0513–692 was seen in the RASS data of the region and also in the Position Sensitive Proportional Counter (PSPC) images. It is listed in the RASS Faint Source Catalogue as 1RXS J051315.7–691219 (Voges et al. 2000) and in the LMC PSPC catalogue by Haberl & Pietsch (1999) as HP 835. Table 3 cites additional information taken from this catalogue.

A useful method to characterize the spectrum of X-ray sources with limited counts is through the calculation of hardness ratios. These (HR1 and HR2) are defined by taking the ratio of the differences in count rates between a set of X-ray energy bands:

$$\text{HR1} = \frac{(\text{hard} - \text{soft})}{(\text{hard} + \text{soft})}, \quad (2)$$

and

$$\text{HR2} = \frac{(\text{hard2} - \text{hard1})}{(\text{hard2} + \text{hard1})}. \quad (3)$$

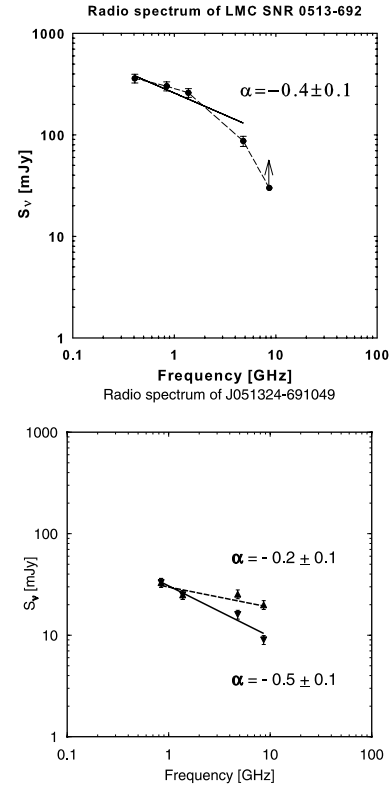


**Figure 4.** Log–log graphs of the radio spectrum from SNR B0513–692 (top panel) and the embedded compact radio source J051324–691049 (bottom panel). The flux density of SNR B0513–692 at 8640 MHz is most likely a lower limit of the actual value and was excluded from the power-law fit. It is more likely that the spectrum of SNR B0513–692 is curved as indicated by the dashed line. No missing flux was detected at higher frequencies (8640/4790 MHz) after comparison with lower-resolution Parkes images. The spectral analysis of J051324–691049 included flux values from the high-resolution image (dashed line) and the low-resolution image (solid line).

In this case, the energy bands are defined as: soft (0.1–0.4 keV), hard (0.5–2.0 keV), hard1 (0.5–0.9 keV) and hard2 (0.9–2.0 keV). SNRs in the LMC have a wide distribution of HR2 values between  $-1$  and  $+0.55$  (Filipovic et al. 1998). The HR2 value for SNR B0513–692 of  $-0.34 \pm 0.17$  (Table 3) is situated very close to the peak of this distribution.

### 3.1.3 Previous and new optical observations

In order to complete our multifrequency discussion of SNR B0513–692, we discuss the previous optical observations of this remnant in more detail. Optical counterparts for SNR B0513–692 have previously been detected in the  $H\alpha$ ,  $[S \text{ II}]$  and  $[O \text{ III}]$  emission lines from AAT narrow-band IPCS image data from Mathewson et al. (1985).

We show in Fig. 5 the new  $[S \text{ II}]$  image of the remnant from the deep MCELS data of the LMC. A  $5 \times 5$ -arcmin<sup>2</sup> area extracted around the position of the radio position of the SNR reveals a coherent, oval shell structure with internal filamentary features but with a strong ‘hint’ of a possible mirror symmetry with two regions with low brightness lying on the major axis. The major and minor axis dimensions are  $245 \times 200 \text{ arcsec}^2$  equating to  $61 \times 50 \text{ pc}^2$  at the distance to the LMC. This grey-scale  $[S \text{ II}]$  image is also overlaid with the 4790-MHz radio contours of Fig. 1 which are seen to be

**Table 2.** Integrated flux densities for SNR B0513–692 and the compact source J051324–691049. Columns 5 and 6 list flux densities for high- and low-resolution images, respectively.

(1) Frequency (MHz)	(2) Noise <sub>rms</sub> (mJy Beam <sup>-1</sup> )	(3) B0513–692 $S_{\nu}$ (mJy)	(4) J051324–691049 $S_{\text{Peak}}$ (mJy Beam <sup>-1</sup> )	(5) J051324–691049 $S_{\nu}$ (high resolution) (mJy)	(6) J051324–691049 $S_{\nu}$ (low resolution) (mJy)
408	—	360.0	—	—	—
843	—	302.0	28.6	—	33.0
1377	0.5	260.0	24.8	—	25.0
4790	0.5	87.0	15.4	16.0	25.4
8640	0.4	30.0	8.4	9.0	19.9

**Table 3.** SNR J0513–692 X-ray data from the *ROSAT* PSPC survey.

RA(J2000)	05 <sup>h</sup> 13 <sup>m</sup> 13 <sup>s</sup> .5
Dec.(J2000)	–69°11′30″
Total positional error	38.7 arcsec
Count rate (counts s <sup>-1</sup> )	1.41 (±0.28) × 10 <sup>-2</sup>
HR1	+1.00 ± 0.42
HR2	–0.34 ± 0.17

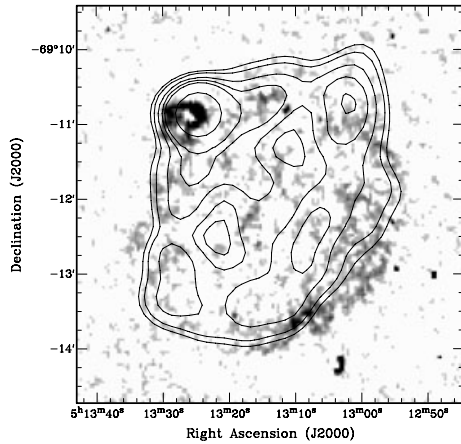


**Figure 5.** Red continuum subtracted 5 × 5 arcmin<sup>2</sup> [S II] image of B0513–692 superimposed with the same 4790-MHz radio contours used in Fig. 1. (MCELS [S II] and red images are provided, courtesy of C. Smith).

well matched in overall extent. This strong optical image from the [S II] 6717/6731 Å emission doublet is indicative of shock-excited gas and a useful diagnostic for SNR optical detection, especially when the [S II] point-to-point emission-line strength is >0.5 times that for H $\alpha$  (e.g. Fesen et al. 1985) as already found by Mathewson et al. (1985).

The equivalent H $\alpha$  image of the SNR taken from the new deep H $\alpha$ /SR (short red) median stacked image of the central 25 deg<sup>2</sup> of the LMC of Reid/Parker (Reid & Parker 2006a,b) is shown in Fig. 6, obtained by dividing the H $\alpha$  image by the matching short-red continuum image. This new H $\alpha$  map has allowed extremely low surface brightness nebulosities and structure to be detected in the vicinity of B0513–692. This is due to its arcsecond resolution and high sensitivity ( $R_{\text{equiv}} \sim 22$  for H $\alpha$  or  $4.5 \times 10^{-15}$  erg cm<sup>2</sup> s<sup>-1</sup> Å<sup>-1</sup>). The H $\alpha$  map is strikingly similar to the [S II] map with all the same, major filamentary features evident within the overall oval structure.

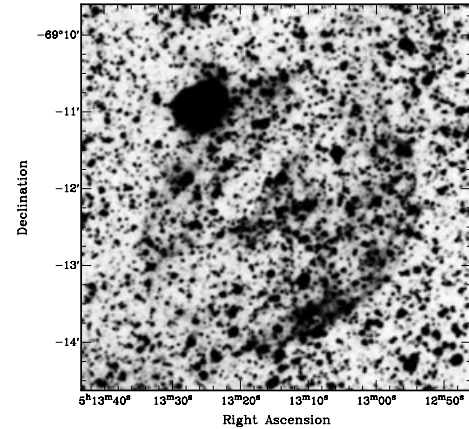


**Figure 6.** A 5 × 5-arcmin-H $\alpha$  divided by short-red (continuum) image of SNR B0513–692 taken from the deep Reid/Parker H $\alpha$  and SR median stacked images of the central 25 deg<sup>2</sup> of the LMC (Reid & Parker 2006a; Reid & Parker 2006b). Note the strong similarity with the equivalent [S II] image from MCELS (Fig. 5) though the compact, strong emission in the north-eastern edge of the SNR is saturated in this presentation, preventing any discernment of internal structure there.

In H $\alpha$  the SNR appears to be a clear example of tilted barrel-shaped morphology (Kesteven & Caswell 1987; Gaensler 1998) with the symmetry axis passing through the bright central filament.

Finally, a new MCELS colour composite H $\alpha$ , [O III] and [S II] image is presented in Fig. 7. This image clearly brings out the nature of SNR B0513–692 and further details concerning the compact region on the north-eastern limb (see Section 3.2 below).

### 3.2 Compact radio source J051324–691049 (optical counterparts LHA 120–N112; DEM L109)

In the north-eastern edge of B0513–692 there is the compact radio source J051324–691049. Previous radio observations of J051324–691049 suggested that it was a compact H II region (Mathewson et al. 1985). An optically identified object at this position was also listed in the Henize (1956) catalogue of Magellanic Cloud emission nebulae as LHA 120–N 112 based on low-dispersion objective prism photographic spectroscopy and as DEM L109 in the catalogue of nebular complexes of the LMCs and SMCs by (Davies, Elliott & Meaburn 1976).

The SIMBAD data base identifiers associated with J051324–691049 are listed in Table 4 and we consider them all as referring to the same source. However, Gurwell & Hodge (1990) listed a galaxy behind the LMC with a position coincident

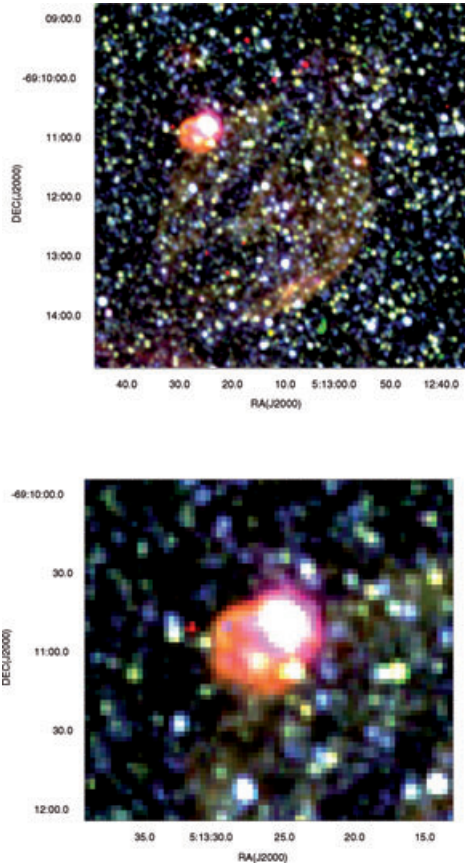


**Figure 7.** Pseudo-colour representations of SNR B0513–692 and J051327–6911. The images are a straight combination of the H $\alpha$  (red), [S II] (green) and [O III] (blue) images obtained by MCELS (courtesy C. Smith). The overall optical morphology and angular size of B0513–692 (top panel) are in good agreement with the new radio images at 3 and 6 cm. The bottom image gives the enlarged north-eastern part of the top image. The bright, orange circular object on the periphery of B0513–692 is clearly distinct both from the large oval shell of B0513–692 itself and from the compact, pink–white H II region immediately to the north-west.

with J051324–691049 based on CTIO 4-m broad-band optical *B* and *V* photometry. They listed coordinates (J2000) of RA = 05<sup>h</sup>13<sup>m</sup>4 and Dec. = –69°11′, citing rather large positional uncertainties of about  $\pm 10^{\circ}$  in RA and  $\pm 1$  to 2 arcmin in Dec. Unfortunately, this led to a confusing connection in the NASA/IPAC Extragalactic Data base (NED) of radio, far- and near-IR coincident

sources with this putative galaxy. Also note that the coordinates of N 112 listed by SIMBAD in Table 4 are incorrect. Here, we provide updated, accurate, optical co-ordinates and attempt to clarify the true nature of the compact N 112 region and its eastern extension through an analysis of new radio, IR, CO and optical data.

### 3.2.1 Radio

The compact radio source, J051324–691049 is embedded within the north-eastern edge of SNR B0513–692. It has a peak flux position at RA = 05<sup>h</sup>13<sup>m</sup>24<sup>s</sup>.8 and Dec. = –69°10′49″.1 (J2000.0). A radio spectral index was constructed using flux densities obtained from our 8640- and 4790-MHz ATCA images and data from other radio frequencies as shown in Table 2. Column 4 lists peak fluxes, column 5 flux densities from our high-resolution images (using all antennas) and column 6 flux densities from our low-resolution images (excluding antenna 6). We use the MIRIAD task IMFIT to determine position and peak/integrated flux values for our data. Flux density values for 843- and 1377-MHz data are the same in both columns 5 and 6.

If we assume that all of the radio flux from J051324–691049 is not fully resolved in the high-resolution imaging process, then the spectral index, fitted from the integrated flux densities (sixth column in Table 2), is relatively flat with  $\alpha = -0.2 \pm 0.1$  as shown by the dashed line in Fig. 4. On the other hand, it is possible that this radio source is unresolved (i.e. if its angular dimensions are less than 1 arcsec beamwidth of the restoring beam used in deconvolution). In this case the spectral index would be strongly non-thermal with  $\alpha = -0.5 \pm 0.1$  as shown by the solid regression line in Fig. 4.

We have calculated the brightness temperature for this compact radio source at 8640 and 4790 MHz using the equation

$$T_B = \frac{\lambda^2 S_\lambda}{2k\Omega_\lambda}, \quad (4)$$

where  $S_\lambda$  is flux density and  $\Omega_\lambda$  is angular size in steradians. The resultant value for  $\lambda \simeq 3.5$  cm is  $T_B^{3.5\text{cm}} = 148$  K and for  $\lambda \simeq 6$  cm is  $T_B^{6\text{cm}} = 213$  K. Since our flux densities at both frequencies represent lower limits, these numbers are also lower limits of brightness temperature. They do not rule out the presence of thermal radio emission from this object.

The polarization estimates for J051324–691049 at each wavelength were found to be below the noise level (i.e. the upper limit for polarization is  $\leq 0.6$  mJy Beam<sup>-1</sup> and  $\leq 0.3$  mJy Beam<sup>-1</sup> for 8640 and 4790 MHz, respectively) and thus not helpful in characterizing radio emission from this object.

**Table 4.** Identifiers from the SIMBAD data base giving previously catalogued objects in the immediate vicinity of the point-like radio source J051324–691049.

Catalogue name	RA(J2000) ( <sup>h</sup> <sup>m</sup> <sup>s</sup> )	Dec.(J2000) ( <sup>°</sup> <sup>'</sup> <sup>''</sup> )	Reference
J051324–691049	05 13 24.8	–69 10 49.1	This paper
LHA 120–N 112	05 13 23.2	–69 11 38.1	Henize (1956)
LHA 120–N 112	05 13 14.6	–69 13 37.0	SIMBAD
DEM L109	05 13 26.5	–69 10 53.3	Davies et al. (1976)
GH 6–2	05 13 24.0	–69 11	Gurwell & Hodge (1990)
IRAS 05137–6914	05 13 24.67	–69 10 48.4	Joint IRAS Working Group
MSX LMC 217	05 13 24.67	–69 10 48.4	Egan et al. (2003)
No. 180	05 13 18.8	–69 10 38	Kawamura et al. (in preparation)
OGLE-CL LMC241	05 13 25.65	–69 10 50.1	Pietrzynski et al. (1999)

### 3.2.2 CO detection as a proxy for molecular hydrogen

We used data from the LMC CO survey undertaken with the 4-m NANTEN millimetre–submillimetre radio telescope<sup>2</sup> (Kawamura et al., in preparation). One of the main aims of the NANTEN project is the full-mapping of molecular clouds in the LMC and along the Galactic plane using the <sup>12</sup>CO(1–0) transition as a proxy for molecular hydrogen. A relatively weak molecular cloud, listed as No. 180 in the LMC CO cloud catalogue was found in the vicinity of J051324–691049. This small molecular cloud (compared to the NANTEN beam of  $\sim 2.7$  arcmin or 39 pc at the LMC distance) was found at (J2000.0): RA =  $05^{\text{h}}13^{\text{m}}17.8$  and DEC =  $-69^{\circ}10'38''$ . The spectrum of the CO emission of this cloud has the absolute antenna temperature,  $Tr^* = 0.49$  K, with a local standard of rest velocity  $V_{\text{lsr}} = 233.4$  km s<sup>-1</sup>, and a full width at half-maximum (FWHM) velocity width of  $\Delta V = 2.34$  km s<sup>-1</sup>. For the LMC NANTEN survey, they take a velocity-integrated intensity,  $\text{II} = 1.2$  K km s<sup>-1</sup> on average, as representing a real detection ( $3\sigma$  noise level). We find only one spectrum towards this region which satisfies the above criteria, though we can ‘see’ the spectrum adjacent to it. If we take a 2-arcmin grid spacing and define a radius ‘ $R$ ’ from the detected cloud area of  $\pi r^2$ , then we find  $R = 16.41$  pc (assuming  $D = 51.5$  kpc). This yields a virial mass  $M_{\text{vir}} = 1.7 \times 10^4 M_{\odot}$ . The observed linewidth of  $2.34$  km s<sup>-1</sup> is one of the narrowest seen among CO emissions in the LMC detected by NANTEN. The average  $\Delta V$  is  $\sim 6$  km s<sup>-1</sup>.

We found that a significant number (>75 per cent) of known LMC SNRs appear to be associated with CO clouds (Kawamura, private communication). This is evidence that the SNR shock front is interacting with the surrounding environment. It is reasonable to expect that most SNRs are located around dense molecular clouds.

However, the question remains as to whether this molecular cloud is physically connected with B0513–692 or indeed associated with another source, given the positional uncertainties of  $\sim 2.7$  arcmin associated with the CO maps. Only higher-resolution CO observations could resolve this question.

### 3.2.3 Infrared and mid-infrared emission

An entry in the *IRAS* Point Source Catalogue, version 2.0 (NASA RP–1190): IRAS B05137 –6914 gave a decent positional match to J051324–691049. Its flux densities in the different *IRAS* bands together with quality measurements, are listed in Table 5. We also note that the *IRAS* observations gave no significant IR emission from SNR B0513–692.

In Fig. 8, we show an 8.3- $\mu\text{m}$  (Band A) high-sensitivity image of J051324–691049 from MSX where the astrometric accuracy permits a much more unambiguous match. The source is seen in all four MSX bands but it is strongest at 8.3  $\mu\text{m}$ . Flux densities from all four bands are listed in Table 5 (Egan et al. 2003). This 8.3- $\mu\text{m}$  MSX image reveals a compact, centre-brightened, but resolved source with an elliptical shape. Its angular dimensions are  $\sim 30 \times 40$  arcsec<sup>2</sup> ( $7.5 \times 10$  pc<sup>2</sup>) and its position, with positional uncertainty of  $\sim 1$  arcsec, is presented in Table 4. The same source is catalogued as record number 20 in the catalogue of cross-correlated LMC sources from MSX and the Two-Micron All-Sky Survey (2MASS) (Egan et al. 2001). Data from matching sources from those two surveys are

**Table 5.** Near-IR and mid-IR flux densities and magnitudes of IRAS 0513–6914 from the MSX, 2MASS and *IRAS* surveys.

Band	Wavelength ( $\mu\text{m}$ )	Integrated flux (Jy)	Magnitude	Survey
–	12.0	0.7824		<i>IRAS</i>
–	25.0	2.584		<i>IRAS</i>
–	60.0	19.71		<i>IRAS</i>
–	100.0	58.1		<i>IRAS</i>
A	8.28	$0.33 \pm 0.01$	5.92	MSX
C	12.13	$0.50 \pm 0.05$		MSX
D	14.65	$0.53 \pm 0.04$		MSX
E	21.34	$1.10 \pm 0.08$		MSX
J	1.0–1.5		$14.7 \pm 0.1$	2MASS
H	1.5–2.0		$14.21 \pm 0.1$	2MASS
$K_s$	2.0–3.0		$13.23 \pm 0.1$	2MASS

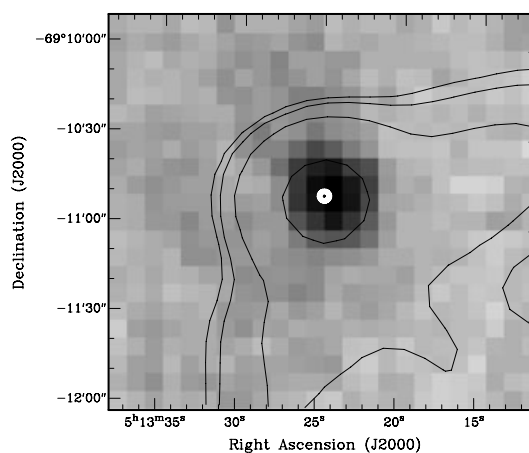


**Figure 8.** MSX 8.3- $\mu\text{m}$  grey-scale image of J051324–691049 overlaid with 4790-MHz low-resolution (black) contours (3, 4, 7 and  $25\sigma$ ;  $\sigma = 0.5$  mJy Beam<sup>-1</sup>) and high-resolution (white) contours (4, 6 and 8 mJy).

presented in order to expand the IR colour baseline. Furthermore, considering the much improved combination of sensitivity and resolution of MSX compared to *IRAS*, better insight into LMC objects with high IR excess (asymptotic giant branch stars, planetary nebulae (PNe) and compact H II regions) is expected. The 2MASS *J*, *H*, *K* survey photometry measured at the J051324–691049 position are also presented in Table 5. The resultant IR colours of the source with  $J - K_s < 2$ ,  $K_s - A \geq 2.5$  and  $0.75 \leq H - K_s < 2$ , J051324–691049 are typical of PNe but also overlap with those of H II regions (Egan et al. 2001). We can resolve the ambiguity between a PN or H II region identification by a simple consideration of the angular extent and hence physical size of J051324–691049 which is estimated at  $\sim 10$  pc, far too large for any PN. This makes a compact H II region the most probable identification. It is most likely powered by the dominant compact stellar association located at the centre of the region which can be seen clearly in the SuperCOSMOS *B*-band image. This stellar content of the H II region is catalogued as the star cluster OGLE-CL LMC241 (Pietrzynski et al. 1999).

### 3.2.4 Narrow-band optical emission-line imaging

To further characterize the nature of the region around the compact radio source we closely examined the new, deep [S II], [O III] and H $\alpha$  images of J051324–691049.

<sup>2</sup> Operated by the Nagoya University at the Las Campanas Observatory in Chile and under mutual agreement with the Carnegie Institution of Washington.

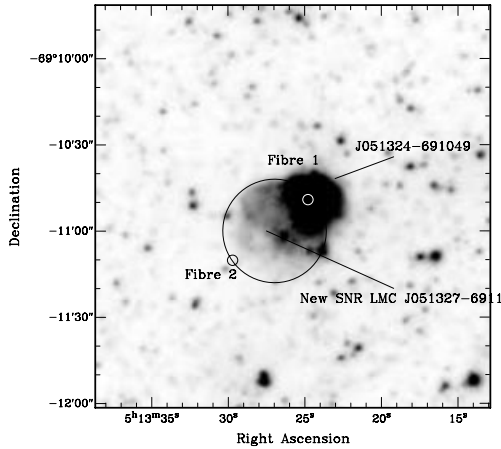


**Figure 9.** AAO/UKST  $12 \times 2$  h exposure median-stack  $H\alpha$  image (gray-scale) of the N112 region (Reid & Parker 2006a,b). The two small circles marked as Fibre 1 (white) and Fibre 2 (black) represent the positions of the two 2dF 2.5-arcsec fibres placed near the centre of J051324–691049 (RA =  $05^{\text{h}}13^{\text{m}}24.8^{\text{s}}$ , Dec. =  $-69^{\circ}10'49''$ ) and on the border of the newly suggested SNR J051327–6911 (RA =  $05^{\text{h}}13^{\text{m}}29.71^{\text{s}}$ , Dec. =  $-69^{\circ}11\text{arcmin}19.2\text{arcsec}$ ) as far away as possible from N113. The larger black circle is centred on the position of the new proposed SNR J051327–6911 and it has an  $H\alpha$  diameter of  $\sim 40$  arcsec. Note that the  $H\alpha$  pixel intensities of this coherent, small, shell-like structure adjacent to the compact  $H\text{ II}$  region are twice that of the strongest optical components of the large oval SNR which are not even visible in this linear grey-scale image adding further support to its distinct nature.

First, we re-examined the red-continuum subtracted MCELS [S II] image of B0513–692 shown in Fig. 5. There is a strong, compact, [S II] emission feature on the north-eastern rim of the SNR that coincides with the compact source J051324–691049. Interestingly, however, there is an additional, quite strong, shell-like feature immediately to the east that blends in to the compact source but appears somewhat distinct compared to the larger, oval structure associated with SNR B0513–692 in terms of emission-line strength and shape.

We have also re-examined data from the  $H\alpha$  map of the LMC referred to in Section 1 (see Reid & Parker 2006a,b for further details) together with the equivalent matching broad-band red ‘SR’ image. This matching  $H\alpha$  image in Fig. 6 has been manipulated to highlight the low surface-brightness coherent details across the whole SNR. Note that the region around the compact  $H\text{ II}$  region N112 is completely saturated in this representation but hints of a two-component nature to the compact saturated zone are seen.

A small extract of the  $H\alpha$  grey-scale image is shown in Fig. 9. Here, the data are shown at base contrast with a linear pixel intensity scale. The compact  $H\text{ II}$  region J051324–691049 is clearly seen as an intense, approximately circular structure about 20 arcsec across but with an irregular border. However, the raw,  $H\alpha$  continuum subtracted image also reveals an adjacent, fainter, approximately circular nebula structure  $\sim 40$  arcsec across and about 15 arcsec to the south-east. We propose that this feature is not simply an extension of the  $H\text{ II}$  region but is a separate source in its own right. This proposition is neatly confirmed when we examine the MCELS combined  $H\alpha$  (red), [O III] (blue) and [S II] (green) image of the region as a colour composite (Fig. 7, bottom panel). The ways the colours combine according to the relative intensity of each emission line highlights the different nature of the various components quite effectively. A clear, very well defined, circular, orange nebula is seen immediately adjacent to the compact pink–white  $H\text{ II}$  region and

clearly brighter than and distinct from the fainter emission levels from the larger-scale B0513–692 remnant. The north-eastern part of B0513–692 intersects with this object across  $\sim 50$  per cent of its area.

We designate this newly identified source as SNR J051327–6911. This new feature also matches the [S II] extension to the compact source seen in Fig. 5.

Despite close angular proximity, the relative  $H\alpha$  and [S II] image intensities and morphologies of the compact radio source J051324–691049 and our newly optically identified proposed SNR J051327–6911, are sufficiently distinct to consider them as separate entities. Unfortunately, the existing radio observations of the region are completely dominated by the flux emanating from the compact  $H\text{ II}$  region so that any independent signal from the adjacent proposed SNR is lost. Further observations with longer integration time and a suitable array configuration to resolve out the area could potentially reveal the radio position and morphology of this object.

### 3.3 Optical spectroscopy of the compact $H\text{ II}$ region and new adjacent SNR candidate

We obtained low-resolution optical spectroscopy of the compact radio source J051324–691049 and the newly suggested adjacent SNR J051327–6911 located 15 arcsec to the south-east (Fig. 9). The

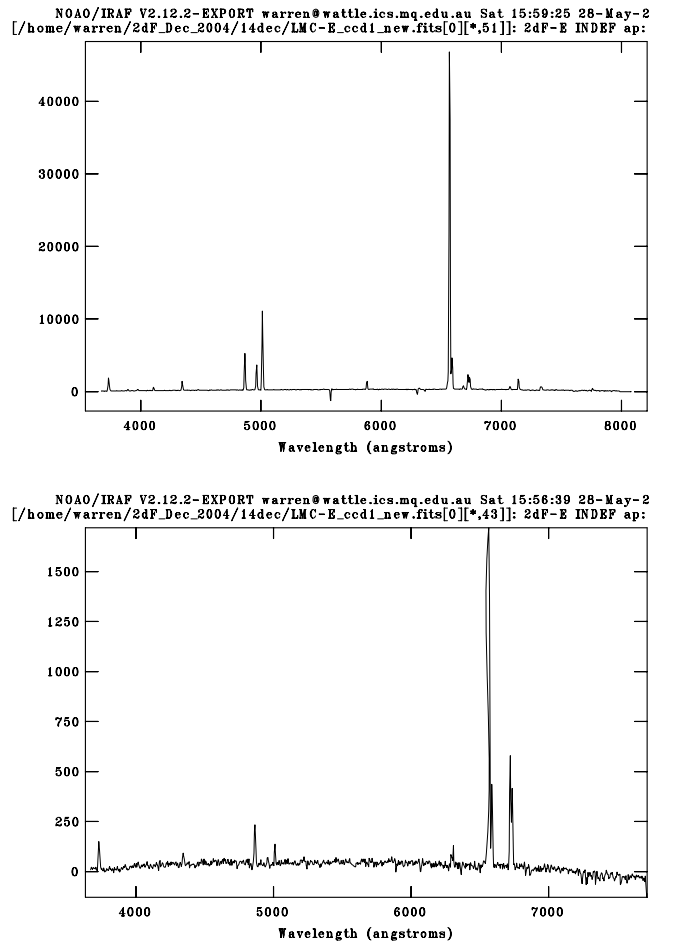


**Figure 10.** 2dF reduced 1D optical spectra of compact radio source J051324–691049 (top panel) and proposed new LMC SNR J051327–6911 (bottom panel). The top spectrum (Fibre 1, Fig. 9) is typical of a galactic  $H\text{ II}$  region, whilst the lower spectrum (Fibre 2, Fig. 9) has strong [S II] lines and prominent [O II] 3727 Å and [O I] 6300, 6363 Å lines typical of an SNR.

**Table 6.** Measured line intensities of compact source J051324–691049 ( $I_{\text{Fibre 1}}$ ) and the new SNR candidate J051327–6911 ( $I_{\text{Fibre 2}}$ ).

$\lambda$ (Å)	Line	$I_{\text{Fibre 1}}$	$I_{\text{Fibre 2}}$
3727	[O II]	22605	1939
3835	H9	618	–
3869	[Ne III]	548	–
3889	[He I]	2153	–
3968	[Ne III]	2571	–
4070	[S II]	4586	–
4340	H $\gamma$	13940	947
4471	[He I]	1419	–
4861	H $\beta$	57374	2704
4959	[O III]	39732	625
5007	[O III]	125190	1004
5876	[He I]	11952	–
6548	[N II]	13849	980
6563	H $\alpha$	517888	18477
6584	[N II]	46554	4360
6678	[He I]	5198	–
6717	[S II]	21016	5901
6731	[S II]	19009	4329
7065	[He I]	4584	–
7135	[Ar III]	15347	–
7323	[O II]	9208	–

spectra were taken with the 2dF multiobject fibre spectroscopy system on the Anglo–Australian Telescope (AAT) in 2004 December as part of an extensive follow-up programme of newly identified LMC emission sources (Reid & Parker 2006b). The reduced, wavelength-calibrated, sky-subtracted, 1D spectra of the two adjacent regions are given in Fig. 10. Note that although no flux calibration was applied, the fibre relative transmissions have been normalized via sky-line flux within the reduction pipeline so that, given the identical exposure times and observing conditions, the relative strengths of H $\alpha$  and other emission lines between the spectra are reasonably indicative. Note that the H II region H $\alpha$  peak intensity is  $\sim 20$  times that of the adjacent source. The measured integrated intensities of the most-prominent lines for both objects as given from Gaussian fits are given in Table 6. As expected, based on the evidence from the multiwavelength images, the optical spectrum centred on the compact radio source J051324–691049 (Fibre 1; Fig. 9 and top panel of Fig. 10) is typical of an H II region or a very low excitation PN due to the absence of high-excitation lines and relatively weak [O III] relative to H $\beta$ . However, as noted previously, a PN is ruled out on the basis of the large physical nebular size. The spectrum of J051327–6911 (Fibre 2; Fig. 9 and bottom panel of Fig. 10) is completely different. The object is clearly not what would be expected if it was from a faint extension to the H II region. Rather it is immediately suggestive of an SNR due to the extremely strong [S II] lines relative to H $\alpha$  and the prominence of the [O II]3727 Å and [O I]6300, 6363 Å emission lines. As shown in Table 7, the measured [S II]/H $\alpha$

**Table 7.** Line intensity ratios at Fibre 1 and Fibre 2 positions.

Lines	Fibre 1	Fibre 2
[N II]/H $\alpha$	0.12	0.29
[S II]/H $\alpha$	0.08	0.55
6717/6731	1.11	1.36

ratio from this spectrum is 0.55 placing it fully within the SNR domain following the line-ratio diagnostics of Fesen et al. (1985). This ratio is a prime indicator for distinguishing SNRs from H II regions, first pioneered for SNR searches in the Magellanic Clouds by Mathewson & Clarke (1973). H II regions typically show [S II]/H $\alpha$  ratios of about 0.1, while SNRs have ratios  $\geq 0.4$  in most galaxies. These new spectroscopic data add significant credence to the veracity of the new SNR identification. The superposition of two SNRs which are likely at different stages of evolution, is rare and provides interesting possibilities for further study. The intersection along the line of sight of SNR B0513–692 and SNR 051324–691049 can be used to test absorption of the closer remnant. With new, better quality spectral line observation in the vicinity of this overlapping region, it may be possible to resolve remaining questions including the interrelation of those two objects. Also, a new, much more sensitive radio observation of these two SNRs could probe the structure of the magnetic field in the interlacing part of the shells through the measure of Faraday rotation.

Electron densities for these two sources calculated from the observed ratio of the [S II] lines are 385.2 and 37.2 cm $^{-3}$  for J051324–691049 and J051327–6911, respectively.

#### 4 INTERACTION BETWEEN THE COMPONENTS

We found no evidence of any interaction between the two SNRs, such as morphology deviation, or enhanced [O III] and X-ray emission at the juncture of the possible colliding region (Williams et al. 1997). Such features are not apparent from the currently available limited observational material. We think that a direct interaction is most unlikely since the young SNR appears just at the rim of the older remnant which is a tight constraint on the position along the line of sight. However, given the short relative lifetimes of SNRs, the two remnants are likely to have exploded at a similar time and space.

There is a possible influence from high-energy UV photons from the nearby star cluster OGLE-CL LMC241 to the ionization of the young SNR, but no stratification of ionized material in the visible part of the shell (outside the H II region) is detected. With appropriate radio observations (wider ATCA configuration and longer integration time), one could construct a distribution of the young SNR spectral index, and map spectral changes across the remnant’s shell. This kind of distribution will show the influence and possible stratification of the thermal emission (from photo-ionization) to the synchrotron radiation as the main radio emission mechanism of an SNR.

According to Elmegreen & Lada (1977), new generations of massive stars in OB associations tend to occur in a sequential manner, that is, star formation moves away from the primordial cloud. Since the young SNR appears centred well outside the nebula, one plausible scenario could be that the progenitor of this remnant belongs to an older generation of nearby massive stars. Perhaps some earlier SN explosions in an earlier cluster triggered star formation in an adjacent molecular cloud. Thus, all three objects (both SNRs and compact H II region) could have originated from the nearby molecular cloud as an evolutionary effect.

#### 5 DISCUSSION AND CONCLUSIONS

We verify B0513–692 as a new SNR but more importantly provide additional radio data and new polarization measurements. Its polarized, steep ( $\alpha = -0.4 \pm -0.1$ ) non-thermal radio emission

and presence of X-ray emission, leave no doubt of its true nature. The existence of a symmetry axis with features like mirror symmetry and low-brightness regions at the end of the axis (see Fig.6), place this remnant in the barrel-shape morphological class (Kesteven & Caswell 1987). Such a variation in the spherical nature of the remnant's structure could be caused by a tube-like structure of the surrounding ISM (Bisnovaty-Kogan, Lozinskaya & Silich 1991) or compression of an ambient magnetic field which generates high-brightness emission regions in part of the shell where shock direction is perpendicular to the vectors of the field (Gaensler 1998). The latter assumption is supported with the measured presence of a relatively strong large-scale magnetic field in this region of the LMC (Gaensler et al. 2005).

Presence of significant polarization suggests that the magnetic fields within the shell are highly ordered and relatively strong. In fact, we find that the estimated level of polarization of this SNR (49 per cent) is among the strongest ever found for an SNR. There is no detected pulsar associated with SNR B0513–692. Available X-ray observations have insufficient spatial resolution and sensitivity to detect an X-ray point source though strong X-ray emission from the remnant was not expected due to its large physical size (Mathewson et al. 1985).

The embedded, compact, radio source J051324–691049, identified previously as an H II region (N 112 or DEM L109) or background source (GH 6-2), is indeed confirmed as a compact H II region, possibly powered by the dominant stellar association, OGLE-CL LMC241, located at its centre. However, there is also an adjacent, faint optical shell seen in both the MCELS [S II] image and the deep, new AAO/UKST H $\alpha$  map of Reid & Parker (2006a,b). It has a diameter of  $\sim 40$  arcsec (10 pc), and is located about 15 arcsec to the south-east of the compact radio source. We consider that this a separate entity which we designate as J051327–6911. The matching [S II] image reveals a strong source at this location compared to the matching faint H $\alpha$  emission, hinting at a likely SNR nature. The subsequent optical spectroscopy for both J051324–691049 and J051327–6911 exhibits markedly different spectral features with the strong [S II] relative to H $\alpha$  for J051327–6911 being indicative of shocked material and having a ratio typical of SNRs. These optical observations combined with its symmetrical structure, which shows a definite boundary, and different optical image intensity, suggests that it is not a part of the more extensive SNR B0513–692. The compact and strong nature of the radio source J051324–691049 most likely prevents any separate signature from this adjacent SNR candidate being seen in the current radio data.

We strongly suggest that J051327–6911 is a new, separate, SNR. Due to the small angular size of this new SNR candidate one would assume a young nature but the lack of a confirmed strong X-ray counterpart of this object could be a strong argument against this presumption though we do propose a possible explanation for the unusually low X-ray brightness of the source. To begin with the existing *ROSAT* PSPC/HRI and Einstein observations are of low integration time and therefore sensitivity. Furthermore, the observations did not cover this area completely (the centre of the both *ROSAT* PSPC and HRI pointings are well away from the new SNR candidate). Another possibility is that this new SNR candidate is interacting with the nearby high-density molecular cloud and that the shock has already decelerated to the point where the gas temperature downstream of the shock is below the X-ray emitting temperature. This reduced X-ray emission could be strongly absorbed along the line of sight (Ye et al. 1995). Finally, the spatial resolution of previous X-ray observations ( $>45$  arcsec) would not be enough to resolve this new and small SNR from the edge of larger nearby

SNR B0513–692. Only new *Chandra/XMM* and deeper ATCA observations of this area may solve true nature of this intriguing object.

The objects are positioned in the Optical Bar and near the kinematical centre of the LMC. There are several H II regions associated with compact groups of young star clusters within  $\sim 150$  pc of the observed field (Yamaguchi et al. 2001) but nothing of the significance and magnitude as the 30 Doradus or N 11 star-forming regions.

Finally, the rare superposition of two SNRs in the LMC at different stages of evolution, but presumably in a similar ISM environment, provides interesting opportunities to unravel any possible interaction and environmental issues through detailed chemical and kinematical analysis.

## ACKNOWLEDGMENTS

We used the KARMA software package developed by the ATNF and the EXSAS/MIDAS software package developed by the MPE. We thank staff at the MSSSO for the help during our optical observations. We also thank Chris Smith for help in obtaining the MCELS images. Many thanks to the anonymous referee for excellent suggestions.

## REFERENCES

- Bisnovaty-Kogan G. S., Lozinskaya T. A., Silich S. A., 1991, *Astron. Soc. Australia Proc.*, 9, 139
- Bock D., Large M., Sadler E., 1999, *AJ*, 117, 1578
- Clarke J. N., Little A. G., Mills B. Y., 1976, *Aust. J. Phys. Astrophys. Suppl.*, 40, 1
- Davies R. D., Elliott K. H., Meaburn J., 1976, *Mon. Mem. Royal Astron. Society*, 81, 89
- Dickel J. R., McIntyre V. J., Gruendl R. A., Milne D. K., 2005, *AJ*, 129, 790
- Egan M. P., Van Dyk S. D., Price S. D., 2001, *AJ*, 122, 1844
- Egan M. P. et al., 2003, *VizieR On-line Data Catalog: V/114* (originally published in: Air Force Research Laboratory Technical Report AFRL-VS-TR-2003-1589)
- Elmegreen B. G., Lada C. J., 1977, *ApJ*, 214, 725
- Feast M., 1999, in Whitelock P., Cannon R., eds, *Proc. IAU Symp. 192, The Stellar Content of Local Group Galaxies. Astron. Soc. Pac., San Francisco*, p. 51
- Fesen R. A., Blair W. P., Kirshner R. P., 1985, *ApJ*, 292, 29
- Filipović M. D. et al., 1998, *A&AS*, 127, 119
- Fukui Y. et al., 1999, *PASJ*, 51, 745
- Fukui Y., Mizuno N., Yamaguchi R., Mizuno A., Onishi T., 2001, *PASJ*, 53, L41
- Gaensler B. M., 1998, *ApJ*, 493, 781
- Gaensler B. M., Haverkorn M., Staveley-Smith L., Dickey J. M., McClure-Griffiths N. M., Dickel J. R., Wolleben M., 2005, *Sci*, 307, 1610
- Gurwell M., Hodge P., 1990, *PASP*, 102, 849
- Haberl F., Pietsch W., 1999, *A&AS*, 139, 277
- Henize K. G., 1956, *ApJS*, 2, 315
- Ho L. C., Ulvestad J. S., 2001, *ApJS*, 133, 77
- Inglis M. D., Kitchin C. R., 1990, *MNRAS*, 246, 358
- Kaler J. B., Jacoby G. H., 1990, *ApJ*, 362, 491
- Kesteven M. J., Caswell J. L., 1987, *A&A*, 183, 118
- Long K. S., Helfand D. J., Grabelsky D. A., 1981, *ApJ*, 248, 925
- Mathewson D. S., Clarke J. N., 1973, *ApJ*, 180, 725
- Mathewson D. S., Healey J. R., 1964, in Kerr F. J., Rodgers A. W., eds, *Proc. IAU Symp. 20, The Galaxy and the Magellanic Clouds. Austr. Acad. of Sciences, Canberra*, p. 283
- Mathewson D. S., Ford V. L., Dopita M. A., Tuohy I. R., Long K. S., Helfand D. J., 1983, *ApJS*, 51, 345
- Mathewson D. S., Ford V. L., Dopita M. A., Tuohy I. R., Mills B. Y., Turtle A. J., 1984, *ApJS*, 55, 189
- Mathewson D. S., Ford V. L., Tuohy I. R., Mills B. Y., Turtle A. J., Helfand D. J., 1985, *ApJS*, 58, 197

- Mills B. Y., Turtle A. J., 1984, Proc. Symp. Structure and Evolution of the Magellanic Clouds, Reidel, Dordrecht, p. 283
- Nelson C. A., Cook K. H., Popowski P., Alves D. R., 2000, AJ, 119, 1205
- Udalski A., Pietrzyński G., Woźniak P., Szymański M., Kubiak M., Żebruń K., 1999, Acta Astron., 49, 521
- Reid W. A., Parker Q. A., 2006a, MNRAS, 365, 401
- Reid W. A., Parker Q. A., 2006b, MNRAS, 373, 521
- Sault R. J., Wieringa M. H., 1994, A&AS, 108, 585
- Sault B., Killeen N., 2004, MIRIAD Users Guide. Aus. Teles. Nat. Fac., Australia
- Weiler K. W., Sramek R. A., Panagia N., van der Hulst J. M., Salvati M., 1986, ApJ, 301, 790
- Williams R. M., Chu Y. H., Dickel J. R., Beyer R., Petre R., Smith R. C., Milne D. K., 1997, ApJ, 480, 618
- van der Marel R. P., Cioni M.-R.L., 2001, AJ, 122, 1807
- Voges A. W. et al., 2000, VizieR On-line Data Catalog: IX/29, <http://vizier.u-strasbg.fr/viz-bin/VizieR?-source=IX/29>
- Yamaguchi R. et al., 2001, PASJ, 53, 985
- Ye T. S., Amy S. W., Wang Q. D., Ball L., Dickel J., 1995, MNRAS, 275, 1218

This paper has been typeset from a  $\text{\TeX}/\text{\LaTeX}$  file prepared by the author.